ON THE MITIGATION OF ATMOSPHERIC PHASE DELAY ARTEFACTS IN INTERFEROMETRIC SAR TIME SERIES

P. Mateus[1], G. Nico[2], R. Tomé[3], J. Catalão[1], and P.M.A. Miranda[1]

[1]*Instituto Dom Luiz, University of Lisbon, Portugal.*
[2]*Istituto per le Applicazioni del Calcolo (IAC), Consiglio Nazionale delle Ricerche (CNR), Bari, Italy.*
[3]*Instituto Dom Luiz, University of Lisbon, and Centro do Clima, Meteorologia e Mudanças Globais, Azores University, Terceira, Portugal.*

ABSTRACT

In this paper, differential maps of total zenith delay (TZD) estimated by GPS and by Weather Research and Forecasting Model (WRF) numerical data are compared with the TZD by Synthetic Aperture Radar (SAR) Interferometry. This maps are generated by processing a set of interferometric SAR images acquired by the ENVISAT-ASAR mission over the Lisbon region from April to November of 2009. To obtain TZD maps from the delay estimated by GPS data, we used MERIS data to fit a parametric model to the empirical variogram, and used the best fit model in the ordinary kriging system of equations. The WRF model is used to model the TZD over the study area at about the same time of SAR acquisitions. The performance of the TZD-GPS and TZD-WRF maps were compared with each other.

Key words: Synthetic Aperture Radar (SAR); SAR interferometry (InSAR); Global Positioning System (GPS); Weather Forecasting and Research System (WRF); Atmospheric phase delay; Total zenith delay (TZD).

1. INTRODUCTION

Synthetic Aperture Radar (SAR) interferometry is a technique that through the measurement of the interferometric phase is able to furnish information about the displacement of terrain or man made structures. This information is useful to study the phenomena causing that displacement, both its spatial distribution and temporal evolution. However, the interferometric phase does not contain only information on geometrical displacement. It is affected also by a temporal delay of the electromagnetic signal caused by temporal changes in spatial distribution refractive properties of the atmosphere which causes a phase delay. This delay introduces a further "displacement" which cannot be distinguished from the one affecting the terrain or the structure to be studied. There are two components of the atmospheric phase delay, a dry component related to atmospheric pressure of dry air and temperature, more stable in time and a wet component related to different atmospheric parameters among which the water vapour fraction in atmosphere, which is much more variable both in time and space. The irregular variations of this last component of atmospheric phase delay are the main causes of atmospheric phase artefacts affecting interferometric SAR applications. In the last few years we conducted different experiments aiming to compare atmospheric phase delay measured by GPS, MERIS sensors and NWM as the WRF weather forecasting system. The experiments were conducted over the Lisbon region where a network of 12 permanent GPS receivers has been installed. The GPS time series of the TZD estimations covers the time interval between the first and last interferogram. We found that the GPS estimates of the TZDs are in good agreement with that computed from WRF numerical data and MERIS data [1]. In particular, the wet component measured by GPS data is well explained in terms of WRF numerical data [2]. In this work we use the results of the above experiments to device a promising strategy to mitigate atmospheric phase delay artefacts in SAR interferograms. A set of 6 ENVISAT ASAR images were acquired during the period from April, 12 to November, 8 2009. The ASAR images were processed in a manner to minimize the temporal baseline resulting in 5 interferograms. Precise orbits were used. The topographic component was removed in all interferograms. Furthermore, in the period this area was not affected by tectonic movements giving rise to large scale terrain deformations. For this reason it is reasonable to assume that the phase measured in each interferogram is mainly related to temporal changes in the atmospheric phase delay properties, especially at large spatial scales. This InSAR dataset was used to quantify the mitigation of atmospheric phase artefacts. Two approaches were chosen to mitigate these artefacts. The first approach is based on the GPS measurements interpolated in space in order to generate a TZD maps to be used in the mitigation operation. The second approach relies on WRF numerical data to compute the TZD maps used to mitigate atmospheric artefacts due to electromagnetic wave propagation. Effectiveness of the above approaches is quantified in terms of a statistical analysis of SAR interferograms before and after the mitigation operation. Advantages and disadvan-

Proc. 'Fringe 2011 Workshop', Frascati, Italy,
19–23 September 2011 (ESA SP-697, January 2012)

tages of the two approaches are discussed also in terms of their operational use.

2. EXPERIMENTAL DATA AND METHODS

2.1. Estimations of TZD from GPS observations

The GPS network consists of 12 permanent stations. Four belonging to the Instituto Geográfico Português (IGP), namely, IGP0, PALM, GRIB and CASC and 7 belonging to Instituto Geográfico do Exercito (IGEOE), namely, CRAI, SMAR, VNOV, ARRA, PARC, MAFR and ALCO. The site FCUL is located at the University of Lisbon campus. The CASC station is also a EUREF station. In this study, the GAMIT (v10.34) software was used to process the GPS data and estimate the atmosphere Total Zenith Delays (TZDs) at the existing stations. We used the Saastamoinen model to estimate a priori values, and Vienna Mapping function 1 (VMF1) in both components [3]. The wet zenith delay for each station was modeled by a piecewise-linear function over the span of the observations. The IGS precise orbits were used in the solution and the cut-off angle chosen for the GPS data was 20 ° [4]. For each site the tropospheric delay corrections were determined every 15 minutes. Rothacher and Mervart [5] recommend 1 estimation about 2-4 h in 24-h observation span for geodetic control surveys. However, the procedure suggested in [5] does not allow to extract all the information about atmosphere contained in GPS data and to compare to InSAR data. For this reason, the TZDs were estimated each 15 minutes to get the TZD at a time as close as possible to that of acquisition on InSAR data. For all the 12 stations, only for the CASC site meteorological data (atmospheric pressure, temperature and relative humidity measured at surface) are available. They were acquired with sampling time of 15 minutes and introduced in the process in the form of met-file. For stations without explicitly introduced values, the standard atmosphere model GPT (Global Pressure and Temperature) is used [6].
Ordinary kriging was evaluated as a procedure for interpolation of TZDs. Ordinary kriging is a linear estimator by which an estimated value of TZD in a particular location can be calculated, from a TZD estimated at other locations, according to the linear combination

$$TZD^*(x) = \sum_{i=1}^{n} w_i TZD(x_i) \qquad (1)$$

where $TZD^*(x)$ is the estimated value of TZD at location x, $TZD(x_i)$ is the observed value of TZD (estimated by GPS data) at location x_i, w_i is the weight given to observed value, x in our case represent the latitude and longitude respectively, and n is the number of observed values. To quantify the Kriging weights w_i, kriging derives the best linear unbiased estimator (BLUE). This property makes kriging an exact interpolator [7]. To solve the ordinary kriging system of equations, necessary to calculate the weights w_i, we apply a common approach, employ what is called a variogram function $\hat{\gamma}(h)$. An estimate of the empirical variogram can be calculated from the equation

$$\hat{\gamma}(h) = \frac{1}{2N(h)} \sum_{i=1}^{N(h)} \left[TZD(x_i) - TZD(x_{i+h})\right]^2 . \qquad (2)$$

In this case, $TZD(x_i)$ and $TZD(x_{i+h})$ are values of the variable TZD estimated by GPS data at locations x_i and x_{i+h}, respectively, separated by a distance h (known as distance lags). To use equation 2 data must be group into pair with similar separation distances of about h distances. Each lag contains $N(h)$ number of pairs. This analysis typically aims at generating an empirical variogram $\hat{\gamma}(h)$ and then fitting a parametric model that adequately captures the structure of the empirical variogram [8, 9]. The success of this task depend of the number of TZDs estimated. The greater the number of data, the greater the statistical reliability in each bin width class. The total number of permanent stations are 12 and only 9 over the same area of the SAR image, this number of stations does not allow the determination of an empirical variogram necessary to fitting a parametric model. To resolve this issue, we used MERIS data to understand the possible parametric models that describe better the spatial distribution of the TZDs. We used the MERIS IWV Level 2 Products with a spatial resolution of 1040×1160 meters, after excluding the pixels with low confidence using the MERIS flags [1]. The IWV values are converted to wet zenith delay using the formula $WZD \approx 6.4IWV$ [10, 11, 12], the days chosen correspond with the acquisition of the SAR images data. Figure 1 show a example of the empirical and parametric variogram for 12 of May, 2009 at approximately 11h UTC. For the 6 days used,

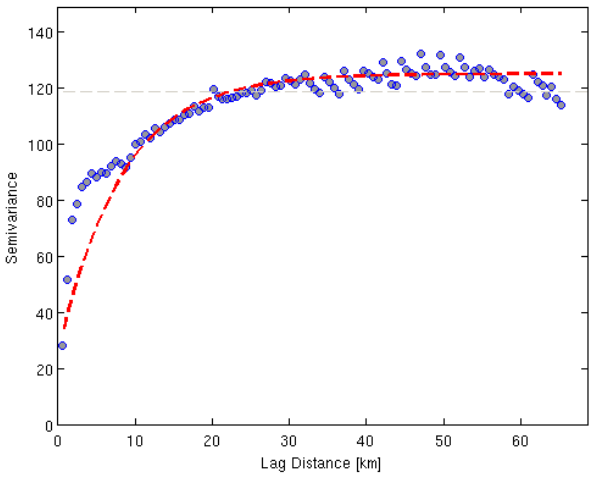

Figure 1. The blue circles represent the empirical variogram, the red dashed line the parametric model and the gray line represents the variation of the sample.

the best fitting model was the exponential model with the

following equation

$$\gamma_{exp}(h) = \begin{cases} 0 & \text{if } |h| = 0 \\ c + \sigma_0^2 \left[1 - exp\left(-\frac{|h|}{a_0}\right)\right] & \text{if } 0 < |h| \end{cases} \quad (3)$$

where the c is the nugget effect, σ_0^2 the partial sill and a_0 the range [7]. This variogram reveal essential information about the wet zenith delay component, and in this case we assumed that the dry zenith delay is eliminated when we do the difference between days because of their stability [2].

2.2. Numerical Weather Models

The Numerical Weather Models (NWMs) are three dimensional models of the lowest part of the atmosphere, from the surface of the Earth up to an altitude of about 30 km approximately. The aim of the NWMs is to predict the future state of the atmosphere from the information on the present conditions by using numerical approximations of the dynamical equations that describe the atmosphere behavior. In this study we used the Weather Research and Forecasting (WRF) Model [13].

2.3. Estimated maps of TZD from the Weather Research and Forecasting Model

The WRF model is a next-generation mesoscale modeling system [13]. A brief description of the physics packages can be found in Skamarock, et al [13]. The model prognostic variables include: In the present study the Advanced Research Weather and Forecasting Model (WRF-ARW) version 3 was setup with a four two-way nested domain at 54, 18, 6 and 1 km horizontal grid resolutions. The top of the atmosphere in the model is located at 10 hPa level, a total of 50 vertical levels are used and the lowest model layer is about 35 m thick. The initial and time-dependent boundary conditions are derived from the ECMWF high resolution analysis. The model contains parameters of temperature, atmosphere pressure and relative humidity required to estimate the TZD. This extends in an area of 280 km in north-south direction and 180 km in east-west direction and a grid of 1 $\times$ 1.2 kilometres. The TZD was calculated by integrating the parameters predict by the WRF model in each one of the profiles using the following equation

$$TZD = 10^{-6} \int N ds, \quad (4)$$

where $N = 10^6(n-1)$ is the refractivity, and n is the refractive index. Following [10], the refractivity can be calculated using atmospheric parameters

$$N = k_1 \frac{P_d}{T} Z_d^{-1} + \left[k_2 \frac{e}{T} + k_3 \frac{e}{T^2}\right] Z_w^{-1}, \quad (5)$$

were $k_1 = 77.604\ K\ mbar^{-1}$, $k_2 = 64.79\ mbar^{-1}$, $k_3 = 3.776 \times 10^5\ K^2\ mbar^{-1}$, P_d is the partial pressure due to dry gases (mbar), T the air temperature (K) and e the water vapor pressure (mbar). The Z_d^{-1} and Z_w^{-1} are the compressibility factors needed to account for the non-ideal behaviour of gases and depending on P_d, T and e [11]. The first term in equation 5, known as the dry or hydrostatic refractivity, does not depend on the atmospheric water vapor content. The second term represents the wet or non-hydrostatic refractivity related to water vapor, the sum of this two components gives the TZD. The last step was geolocated the TZD maps to the same grid as the interferograms.

2.4. Interferometric SAR processing

A set of 6 interferometric ENVISAT-ASAR images, covering the city of Lisbon (Portugal) and surrounding areas, was used. They were acquired from 12 of April to 08 of November of 2009 along the ascending pass. The DORIS software (Delft University of Technology) was used for interferometric processing. Before the phase unwrapping, the interferometric data were multilooked by 40 $\times$ 8 pixels to reduce phase noise [14].
After phase unwrapping we can derived the differential TZD from the following equation

$$\Delta TZD = -\frac{\lambda}{4\pi} \Delta\varphi M_f, \quad (6)$$

where ΔTZD is the differential TZD, λ is the radar wavelength, $\Delta\varphi$ the interferometric phase, $M_f = 1/cos(\vartheta_{inc})$ is the mapping function and ϑ_{inc} is the radar incidence angle [4]. In the process of phase unwrapping an arbitrary constant is introduced in $\Delta\varphi$ that passes to ΔTZD maps, for this reason this maps was to be calibrated using GPS data. For this task we used the methodology described by Mateus, et al [15, 16]. The calibration process, takes into account that about 50% of de wet delay originates from the lower 1.4 km of the tropospheric layer [4] and the used cut-off elevation angle of 20 $^\circ$ in the GPS processing, forms a cone with the receiver in the focal point. The intersection of this cone and the 1.4 km level form a circle with a diameter of 7.6 km. It was assumed that the main contribution to the GPS wet delay comes from atmosphere within this cone. We averaged all TZDs values of interferogram pixels lying within this circle before comparing InSAR measurement of TZD to GPS values.

3. DATA ANALYSIS AND RESULTS

We generated TZDs maps in correspondence with SAR images acquisitions, firsts based on GPS estimates of the TZD, for this task we used the ordinary kriging interpolation and MERIS data to fit the better parametric model to the empirical model, the intent of this procedure is characterize the spatial continuity or roughness of a data set. In second place, based in the parameters predict by the WRF model applying equation 4. All these maps are geolocated at interferometric grid. Figure 4 displayed in the

Table 1. Pearson correlation coefficient between the TZD maps generated by InSAR and the estimated by GPS and WRF data. The standard deviation of all InSAR-TZD maps before and after removal of the GPS and WRF values.

	Correlation coefficients		Standard deviation (mm)		
Interferograms	GPS	WRF	InSAR (original)	GPS (after)	WRF (after)
M0517-S0412	0.85	0.37	10.9	5.9	6.7
M0517-S0621	0.90	0.93	21.4	9.5	15.8
M0726-S0621	0.61	0.91	20.0	10.3	16.5
M1004-S0830	0.21	0.26	12.7	8.2	9.0
M1004-S1108	0.42	0.33	15.6	7.2	7.4

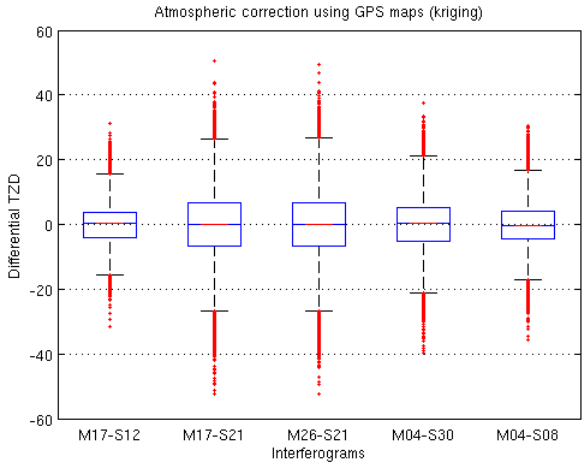

Figure 2. Boxplot indicating the degree of dispersion (spread) and skewness in the data, and identify outliers. The abscissa identifies the interferogram after removal of the TZD-GPS maps. Values in mm.

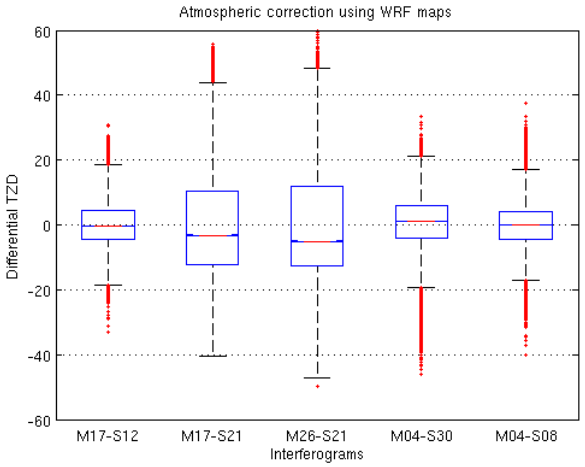

Figure 3. Boxplot indicating the degree of dispersion (spread) and skewness in the data, and identify outliers. The abscissa identifies the interferogram after removal of the TZD-WRF maps. Values in mm.

first column the TZD maps generated by InSAR, the second column shows the TZD maps estimated by GPS data and the last column by the WRF numerical data. Both techniques captured the trend in the spatial distribution of the InSAR maps. Statistical test (Kolmogorov-Smirnov test) confirm that the TZD-GPS and TZD-InSAR differential maps show the same probability distribution for a significance level of 10%, is not the case of the TZD-WRF maps, it can be seen that the TZD-WRF maps has a lower variability than the InSAR and GPS maps. The two data anyway reproduce similar features and show a high correlation except the M1004-S0830 in both cases, see table 1. Figure 5 show the TZD-InSAR maps after removal of the TZD-GPS and TZD-WRF values, first and second column, respectively. Figure 2 and 3 shows the dispersion of the final TZD-InSAR maps, and the outliers. All cases have more that 3% of values identified as outliers, this can reveal the presence of noise in the interferometric phase. Table 1 show the variation of the standart deviation before and after correcting for GPS and WRF data. In each case, GPS and WRF data are able to reduce the values dispersion. We can see from figures 2, 5 and table 1 that TZD maps interpolated from GPS data (using the methodology described in section 2.1) shows a better mitigation that WRF numerical data.

4. CONCLUSIONS

In this paper, we experimentally analyse the capability of the GPS and WRF numerical data to mitigate atmosphere artefacts present in SAR interferograms. The first conclusion that we can draw from these results, GPS data are in better agreement with the TZD maps derived from the InSAR interferograms than WRF forecasts. However, the methodology described in section **??**, needs further study, fitting a theoretical model should aim to capture the major spatial features. The exponential model tested against the empirical variogram is the best fit to all of the 6 days. The result mean squared error and the possibility of using nested models has to be evaluated. This results can be

useful in small areas and/or a few GPS stations. In this five examples both techniques GPS and WRF model succeeded in mitigation of most part of the atmosphere artefacts in SAR interferograms. When compared, the GPS have better results, and the possibility of adding new GPS and meteorological stations can increase the accuracy of the kriging system. Until now, this process is much faster than using the WRF numerical data duo to its complexity and resources needed to implement it. Therefore, at the moment WRF is the best alternative when there is no GPS data or the study area is a large scale.

REFERENCES

[1] Mateus, P., Nico, G. and Catalão, J. (2010), Interpolating MERIS and GPS measurements of precipitable water vapour (PWV) to estimate atmospheric phase delay maps. Proceedings of SPIE Vol. 7827, 782713.

[2] Mateus, P., Nico, G., Tom, R., et al. (2010), Comparison of precipitable water vapor (PWV) maps derived by GPS, SAR interferometry, and numerical forecasting models. Proceedings of SPIE Vol. 7827, 782714.

[3] Boehm, J. B. Werl, and Schuh, H. (2006), Troposphere mapping functions for GPS and very long baseline interferometry fromEuropean Centre for Medium-Range Weather Forecasts operational analysis data. J. Geophys. Res., 111, B02406, doi:10.1029/2005JB003629.

[4] Hanssen, R. F. (2001), Radar Interferometry, Data Interpretation and Error Analysis. Delft University of Technology, Netherlands. ISBN 0-7923-6945-9.

[5] Rothacher, M., and Mervart L. (1996), Bernese GPS Software Version 4.0. Astronomical Institute, University of Berne, Switzerland.

[6] Herring, T. A., King, R. W. and McClusky, S. C. (2006), Documentations for the GAMIT, Reference Manual, GPS Analysis at MIT. Department of Earth, Atmospheric, and Planetary Sciences Massachusetts Institute of Technology. Release 10.3.

[7] Wim C.M. van Beers and Jack P.C. Kleijnen (2004), Kriging interpolation in simulation: a survey. Proceedings of the 2004 Winter Simulation Conference R .G. Ingalls, M. D. Rossetti, J. S. Smith, and B. A. Peters, eds.

[8] Atkinson P. and Lloyd C. D. (1998), Mapping Precipitation in Switzerland with Ordinary and Indicator Kriging. Journal of Geographic Information and Decision Analysis, vol. 2, no. 2, pp. 65-76.

[9] Daly, C., Neilson, R. P. and Phillips, D. L. (1994), A statistical-topographic model for mapping climatological precipitation over mountainous terrain, Journal of Applied Meteorology, 33; 140158.

[10] Davis, J.L., Herring, T. A., Shapiro, I. I., Rogers, A. E. E., Elgered, G. (1985), Geodesy by radio interferometry: Effects of atmospheric modeling errors on estimation of baseline length, Radio Sci., 20, 1593-1607.

[11] Mendes, V. (1999), Modeling the neutral-atmosphere propagation delay in radiometric space techniques, Ph.D. dissertation, Department of Geodesy and Geomatics Engineering, Technical report No. 199, University of New Brunswick, Fredericton, New Brunswick, Canada, 353 pp.

[12] Bevis, M., S. Businger, and S. Chiswell. (1994), GPS meteorology: Mapping zenith wet delays on to Precipitable water, J. Appl. Meteorol., 33, 379386.

[13] Skamarock W.C., J.B. Klemp, J. D. D. G. D. B. M. D. X. H. W. W. and Powers, J. (2008), A description of the advanced research wrf version 3. NCAR Tech Note 475 , Natl. Cent. for Atmos. Res., Boulder, Colorado.

[14] G. Nico, G. Palubinskas, M. Datcu. (2000), Bayesian approaches to phase unwrapping: theoretical study. IEEE Transactions on Signal Processing, 48(9): 2545-2556.

[15] Mateus, P., Nico, G., Catalão, J. Can SAR interferometry be used to study the temporal evolution of PWV?, IEEE Transactions on Geoscience and Remote Sensing, (in press).

[16] Mateus, P., Nico, G., Catalão, J. (2010), Mapping temporal evolution of water vapour in troposphere by interferometric SAR data. Proceedings of SPIE Vol. 7827, 782712.

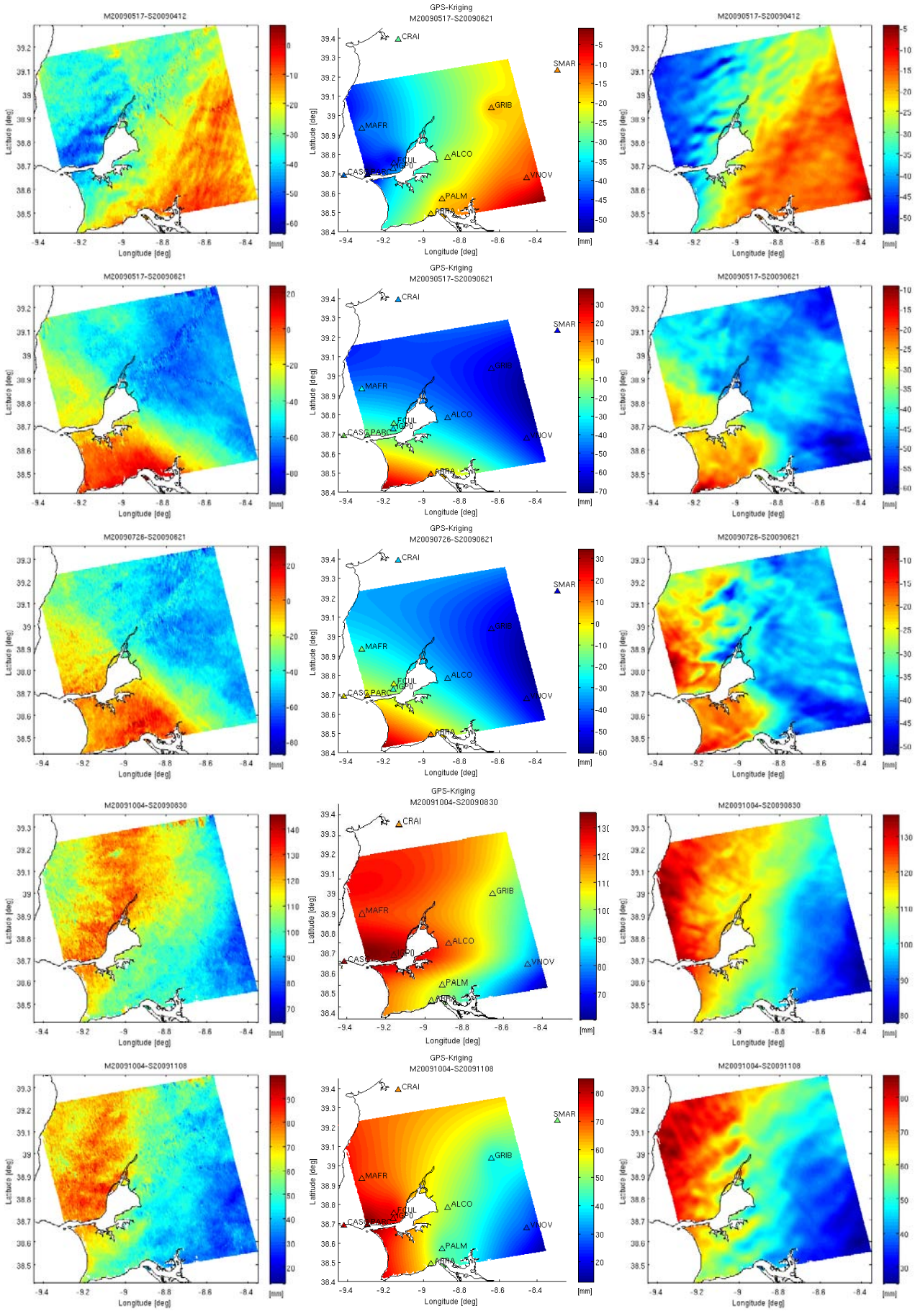

Figure 4. The first column shows TZD maps derived from the interferograms. The second column shows the differential TZD estimated using GPS data, the colour of the triangles represents the value estimated by the GPS measurements at actual scale. The last column shows differential maps derived from WRF numerical data. Other: 1)M0517-S0412 2)M0517-S0621 3)M0726-S0621 4)M1004-S0830 and 5)M1004-S1108. All values are in mm.

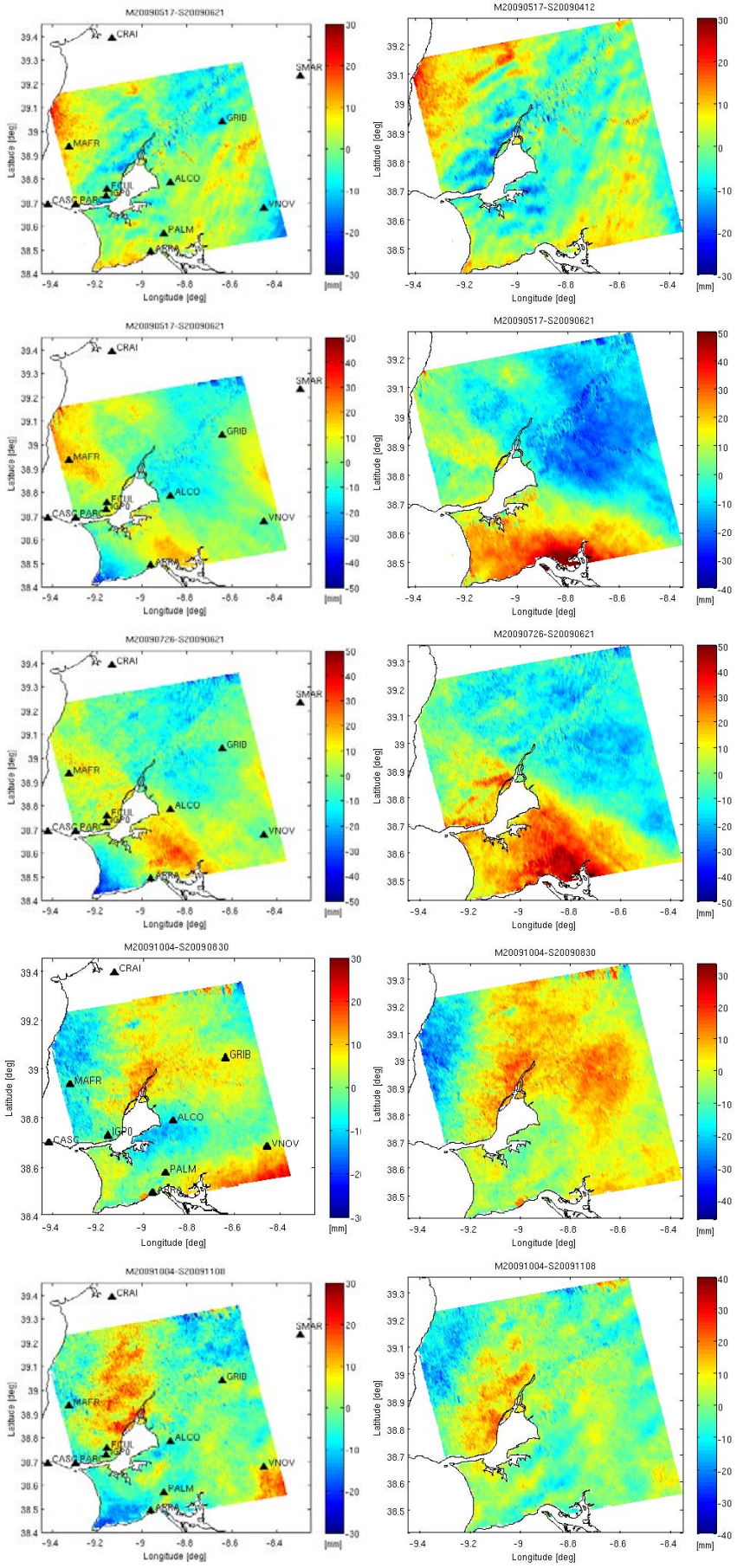

Figure 5. The first column shows the differential TZD derived from InSAR after removal of the TZD-GPS values, the blacks triangles show the location of the GPS permanent stations. The second column shows the differential TZD derived from InSAR after removal of the TZD-WRF values. Other: 1)M0517-S0412 2)M0517-S0621 3)M0726-S0621 4)M1004-S0830 and 5)M1004-S1108. All values are in mm.